

A SPECTROSCOPIC SAMPLE OF MASSIVE, EVOLVED $z \sim 2$ GALAXIES: IMPLICATIONS FOR THE EVOLUTION OF THE MASS-SIZE RELATION¹

J.-K. KROGAGER^{2,3}, A. W. ZIRM², S. TOFT², A. MAN², G. BRAMMER^{3,4}

Accepted for publication in ApJ October 7, 2014

ABSTRACT

We present deep, near-infrared *HST*/WFC3 grism spectroscopy and imaging for a sample of 14 galaxies at $z \approx 2$ selected from a mass-complete photometric catalog in the COSMOS field. By combining the grism observations with photometry in 30 bands, we derive accurate constraints on their redshifts, stellar masses, ages, dust extinction and formation redshifts. We show that the slope and scatter of the $z \sim 2$ mass-size relation of quiescent galaxies is consistent with the local relation, and confirm previous findings that the sizes for a given mass are smaller by a factor of two to three. Finally, we show that the observed evolution of the mass-size relation of quiescent galaxies between $z = 2$ and 0 can be explained by quenching of increasingly larger star-forming galaxies, at a rate dictated by the increase in the number density of quiescent galaxies with decreasing redshift. However, we find that the scatter in the mass-size relation should increase in the quenching-driven scenario in contrast to what is seen in the data. This suggests that merging is not needed to explain the evolution of the median mass-size relation of massive galaxies, but may still be required to tighten its scatter, and explain the size growth of individual $z = 2$ galaxies quiescent galaxies.

Keywords: galaxies: formation — galaxies: high-redshift — cosmology: observations

1. INTRODUCTION

Over the past decade, studies of the $z \sim 2$ Universe have been revolutionized by the availability of deep near-infrared (NIR) imaging surveys. One of the primary early results was the discovery of a population of optically-faint, massive galaxies which are missed in optical (rest-frame UV) surveys (Franx et al. 2003; Daddi et al. 2004; Wuyts et al. 2007). Large photometric surveys have since shown that at $z = 2$, roughly half of the most massive ($\log M/M_{\odot} > 11$) galaxies are dusty and star-forming, and half are old, quiescent systems (e.g. Franx et al. 2008; Toft et al. 2009; Williams et al. 2010; Brammer et al. 2011), a result that has been confirmed through low resolution spectroscopy of a small sample of the brightest examples (Kriek et al. 2008, 2009a,b).

Using high-resolution NIR imaging, it was shown that most of the quiescent galaxies at $z > 2$ have effective radii, r_e , a factor of 2 – 6 smaller than local elliptical galaxies with the same stellar masses (e.g., Daddi et al. 2005; Trujillo et al. 2006; Zirm et al. 2007; Toft et al. 2007; Buitrago et al. 2008; van Dokkum et al. 2008; Szomoru et al. 2010; Cassata et al. 2011; Bruce et al. 2012; Newman et al. 2012). Their inferred stellar mass densities (within r_e) therefore greatly exceed those of local galaxies at the same stellar mass. However, recent studies show that if one compares the stellar densities within the inner 1 kpc the discrepancy is much less pronounced (Bezanson et al. 2009; Patel et al. 2013). The discovery that the inner regions of these massive galax-

ies correspond well with their local counterparts supports the so-called *inside-out* scenario, in which galaxies form at high redshift as compact galaxies presumably from a gas rich merger funneling the gas to the center and igniting a massive, compact star burst (e.g., Hopkins et al. 2006; Wuyts et al. 2010). These resulting compact stellar cores subsequently grow by adding mass to their outer regions. How this size growth is accomplished is the big question; A cascade of merger events with smaller systems, known as minor merging, is a plausible explanation as simulations have shown that it is possible to obtain the needed mass increase in the outer regions while leaving the central core mostly intact (Oser et al. 2012). However, observations of the merger rate of massive galaxies between $z = 2$ and 0 do not find as many mergers as required to account for the observed size evolution (Man et al. 2012; Newman et al. 2012).

Some studies of high-redshift, quenched galaxies have suggested that their structure may differ from that of local elliptical galaxies when quantified using a Sérsic profile. Chevance et al. (2012) find that the high- z galaxies show lower Sérsic indices ($n \sim 2$ on average) than the local population of ellipticals ($n \sim 4$), see also Weinzirl et al. (2011). This is further supported by the detection of galaxies at redshift $z \sim 2.5$ with apparently disc-like morphologies (Stockton et al. 2004, 2008). This has motivated suggestions that the high- z population might be more disc-like and hence might contain a faint, extended stellar component which would be undetected in present observations due to cosmological surface-brightness dimming (van der Wel et al. 2011). Deeper and higher resolution imaging, along with image stacking, has confirmed that the massive, red galaxies indeed are compact, and has failed to detect any extended stellar haloes around these compact cores (van Dokkum et al. 2008, 2010). Moreover, Szomoru et al. (2012) find Sérsic indices for galaxies at high redshift ($z \sim 2$) consistent with the lo-

¹ Based on observations carried out under programs #12177, 12328 with the Wide Field Camera 3 installed on the *Hubble Space Telescope*.

² Dark Cosmology Centre, Niels Bohr Institute, University of Copenhagen, Juliane Maries Vej 30, DK-2100 Copenhagen O

³ European Southern Observatory, Alonso de Córdova 3107, Casilla 19001, Vitacura, Santiago, Chile

⁴ Space Telescope Science Institute, 3700 San Martin Drive, Baltimore, MD21210, USA

cal values. They report a median value for the Sérsic indices at high redshift of $n = 3.7$.

Now, with the advent of the next generation of NIR spectrographs on 8-m class telescopes, we can study the stellar populations via continuum detections and absorption line indices (Toft et al. 2012; Onodera et al. 2012; van de Sande et al. 2013; Belli et al. 2014a,b, Zirm et al. in prep); The quiescent galaxies can be further sub-divided into post-starbursts (those that show strong Balmer absorption lines) and more evolved systems with metal absorption lines. However, even with state-of-the-art instrumentation, target samples are limited to the rare and bright examples.

Grism spectroscopy from space with *Hubble Space Telescope* (*HST*) allows us to obtain redshifts for fainter, less massive examples of $z \sim 2$ galaxies. While these data have poor spectral resolution, they do not suffer from the strong atmospheric emission lines, poor transmission and bright background that limit ground-based observations. A near-infrared spectroscopy survey, 3D-HST, has recently been carried out using the Wide Field Camera 3 (WFC3) onboard the *HST*. The survey provides imaging in the F140W-band and grism observations in the G141 grism. In total the survey provides rest-frame optical spectra of ~ 7000 galaxies in the redshift range from $z = 1 - 3.5$. Moreover, the pointings cover approximately three quarters of the deep NIR survey, CANDELS (Grogin et al. 2011; Koekemoer et al. 2011). The combination of imaging and spectroscopic data from 3D-HST and CANDELS allows for powerful analysis of the redshift $1 < z < 3.5$ Universe. For more details about the 3D-HST survey, see Brammer et al. (2012).

Until now, spectroscopic samples of quiescent, high-redshift galaxies with structural data have been sparse; van Dokkum et al. (2008) presented a sample of nine galaxies at $z \sim 2$, Gobat et al. (2013) presented five quiescent galaxies from a proto-cluster at $z = 2$, Tanaka et al. (2013) presented spectroscopy of a $z = 2.16$ proto-cluster with four quiescent members, and recently Belli et al. (2014b) presented a sample of 6 quiescent galaxies at $2 < z < 2.5$. At slightly lower redshifts Onodera et al. (2012) presented sample of 18 quiescent galaxies at $z \sim 1.6$ and Belli et al. (2014a) presented a large sample of 103 galaxies with redshifts $0.9 < z < 1.6$. Samples of $z \sim 2$ quiescent galaxies with measured velocity dispersions and dynamical masses are even smaller; so far only a handful of examples have been published (van Dokkum et al. 2009; Onodera et al. 2010; van de Sande et al. 2011; Toft et al. 2012; Belli et al. 2014b).

We have compiled a mass-complete sample ($\log(M/M_{\odot}) > 10.8$) of galaxies in the COSMOS region of the 3D-HST survey. By matching the photometric sample of galaxies to the spectra extracted from the 3D-HST data we can improve the redshift determinations compared to the photometric redshifts used so far. By inferring sizes, redshifts, and stellar population parameters including age, star-formation rate, and mass, we are able to populate the mass-size relation using a mass-complete, quiescent sample of galaxies at $z \sim 2$. This provides strong constraints on what drives the size evolution of the massive galaxies. We explore different physical explanations for the apparent size growth. Specifically, we create a simplistic model to investigate

the effect of progenitor bias, i.e., addition of newly quenched, larger galaxies to the mass-size relation, a mechanism proposed by previous studies (Cassata et al. 2011; Trujillo et al. 2012; Poggianti et al. 2013) and recently investigated in detail out to redshift $z \sim 1$ by Carollo et al. (2013).

The paper is organized as follows: In section 2 we present the data used in our analysis, in section 3 we describe the selection of our sample before presenting the results of our analysis in section 4 and 5, in section 6 we investigate the mass-size relation and describe our model for size evolution driven by quenching, and finally we discuss the implications in section 7.

Throughout this paper, we assume a flat cosmology with $\Omega_{\Lambda} = 0.73$, $\Omega_m = 0.27$ and a Hubble constant of $H_0 = 71 \text{ km s}^{-1} \text{ Mpc}^{-1}$.

2. DATA

The analysis is based on public grism spectroscopy data from the 3D-HST survey from which we have used 25 pointings in the COSMOS field. We have combined the spectroscopic data with photometric data in 30 bands covering $0.15 - 24 \mu\text{m}$ from the latest K_s -selected catalog by Muzzin et al. (2013).

The 25 pointings in COSMOS are covered by imaging in the F140W filter and by NIR spectroscopy using the G141 grism providing wavelength coverage from $1.1 \mu\text{m}$ to $1.6 \mu\text{m}$ with a spectral resolution of $R \sim 130$ (for a point source) with a sampling of 46.5 \AA per pixel. Since these are slitless spectroscopic data the effective resolution depends on the size and morphology of the dispersed source. This results in an effective resolution of the order of $R \sim 50$ due to morphological broadening. Furthermore, we have used the structural parameters from van der Wel et al. (2012) obtained from the WFC3/F160W (H_{160}) images as part of the public CANDELS survey (Grogin et al. 2011; Koekemoer et al. 2011).

2.1. Data reduction

Each pointing was observed in a four-point dither pattern with half-pixel offsets in order to increase the resolution of the final image. Both the undispersed, direct images and the dispersed grism images were observed with this pattern for a total exposure of around 800 sec and 4700 sec for undispersed and dispersed, respectively.

The data sets were reduced using the publicly available pipeline *threedhst*⁵ (Brammer et al. 2012). The pipeline handles the combination and reduction of the dithered exposures, source identification using SExtractor, and extraction of the individual spectra. Since we are dealing with slitless spectroscopy some sources will have spatially overlapping spectra. This is handled in the pipeline and each extracted spectrum is provided with an estimate of the amount of contamination from nearby sources. For our analysis, we have subtracted the contaminating flux from the total extracted flux.

We have used the standard extraction parameters in the pipeline except for the final pixel scale used in the call to the IRAF-task MULTIDRIZZLE, where we chose $0''.09 \text{ px}^{-1}$ instead of $0''.06 \text{ px}^{-1}$. This was chosen to reduce the noise in the extracted spectra. For further

⁵ <http://code.google.com/p/threedhst>

details about the observations and data reduction see Brammer et al. (2012). We used a detection threshold of 4σ to identify sources in the F140W images.

After the initial reduction we encountered some issues with the background not being flat. We were not able to correct this gradient sufficiently to recover a completely flat background, which meant that some spectra were disregarded due to background issues. However, when we increased the pixel size from $0''.06 \text{ px}^{-1}$ to $0''.09 \text{ px}^{-1}$ the noise decreased and the background subtraction was performed more successfully. In the process of selecting our sample we removed three sources due to background-subtraction issues. In these cases (IDs #133915, #133784, and #207144) there were discontinuities in the background, that we could not correct for. See appendix A for details.

3. SAMPLE SELECTION

We selected all sources in the survey area (25 pointings in the COSMOS field from the 3D-HST survey) from a mass complete sample by Muzzin et al. 2013 with stellar masses larger than $\log(M_*/M_\odot) > 10.8$. Only sources with photometric redshifts in the range of $1.85 < z_{\text{phot}} < 2.3$ were included in order to sort out low-redshift interlopers. The redshift cut ensured that the 4000 Å break will be visible in the spectra, as this is the only strong spectral feature available at this resolution and wavelength coverage. In total we have 34 galaxies above the mass limit with photometric data.

The photometric targets were then matched by coordinates to the catalog of extracted sources in the 3D-HST data. Next step was to sort out incomplete spectra. We required that at least 80 per cent of the pixels be well-defined, i.e., non-zero and non-negative. In some cases where the objects were located close to the edge of the CCD some light was dispersed out over the edges, and hence the spectral range was reduced in those cases. By only allowing spectra with more than 80 per cent well-defined pixels, we ensured that our targets were fully covered in the wavelength range from 1.1–1.6 μm . For each spectrum, we calculated the median SNR per pixel. We discarded two targets (IDs #123780 and #124168) with a median SNR per pixel less than 1, i.e., more than half of the pixels were heavily noise dominated.

The sources with spectra were then scaled to the J -band flux, which is fully covered by $G141$. Sources whose J -band flux could not be calculated due to too many noisy pixels within the J -band wavelength coverage were discarded. We scaled the spectra to account for the loss of flux due to the limitations of the spectral extraction aperture. Finally, we checked how well the contamination (if any) had been subtracted. We discarded the most heavily contaminated spectra and the spectra where the contamination had been subtracted incorrectly leaving gaps and holes in the extracted spectra. This was done by visual inspection as not only the amount of contamination is important, but also the shape of the contaminating flux. In some cases the contaminating flux can enhance or even create a break in the spectrum, and this is difficult to quantify in a comparable way for all targets.

In the end we end up with a spectroscopic sample of 14 galaxies. The properties of the full sample consisting of 34 galaxies (of which 14 have spectral data available) are summarized in Table 1. In appendix A, we give a list

of the spectra that were discarded along with remarks on why they were removed from our sample.

3.1. Quiescent versus Star-Forming

Since we only wish to study the quiescent population, we need a method to distinguish between star-forming and quiescent galaxies. For this we use the so-called UVJ selection, based on the rest-frame $U-V$ and $V-J$ colours following Williams et al. (2009). The rest-frame colours for our sample are included in the catalog from Muzzin et al. (2013). The classification from the UVJ criteria is given for each sample member in Table 1: 'QG' for quiescent galaxies and 'SFG' for star-forming galaxies.

In Sect. 4, we will analyse the spectral energy distributions (SEDs) and compare the UVJ -classification with the star formation rates inferred from the SEDs.

3.2. Spectral completeness

In the process of discarding galaxies from the photometric sample based on their available spectra we may have introduced biases in the final spectroscopic sample, e.g., the sizes and masses may be systematically underestimated due to low SNR and faint sources being discarded. In this section, we address the selection effects. We perform a Kolmogorov-Smirnov (KS) test on the distributions of masses, sizes and H -band magnitudes comparing the spectroscopic sub-sample to the full photometric sample, the details as to how we infer masses and sizes are described in Sect. 4 and 3. In Fig. 1, we show the distributions of stellar mass, circularized effective radii and H -band AB magnitudes for quiescent and star-forming galaxies. In each panel, we give the calculated KS statistic along with the p value. All distributions are fully consistent with being drawn from the same distribution, and hence no significant bias is introduced in the spectroscopic selection. Nevertheless, we do note that the spectroscopic selection for the quiescent galaxies seems to exclude the faintest sources with $H > 22.25$. However, this does not translate into a bias in the inferred masses and sizes. On the other hand, the brightest star-forming galaxies seem to be discarded by the spectroscopic selection. This may be explained by the star-forming galaxies on average being more extended and thus having their flux distributed among more noisy pixels, thereby lowering the SNR in the spectrum.

4. SPECTRAL FITTING

All galaxies in our sample were fitted by the FAST code (Kriek et al. 2009b) using their photometry and photometric redshifts only. The code performs template fitting combining the photometric data with our grism spectra using exponentially declining star-formation histories (with $\log(\tau)$ from 7.0 to 9.9 in steps of 0.1), stellar population synthesis models by Bruzual & Charlot (2003) and a Chabrier (2003) initial mass function. All fits (both with and without spectra) were performed with variable metallicity among four discrete values: $Z = 0.004, 0.008, 0.02, 0.05$. We used templates with a grid of ages from $7.5 < \log(\text{age}/\text{yr}) < 9.7$ in steps of 0.1, and always less than the age of the Universe at the given redshift, and with a grid of dust attenuation of $0 < A_V < 2.5$ in steps of 0.1. The subsample of sources with spectra were then fitted again with the added spectral informa-

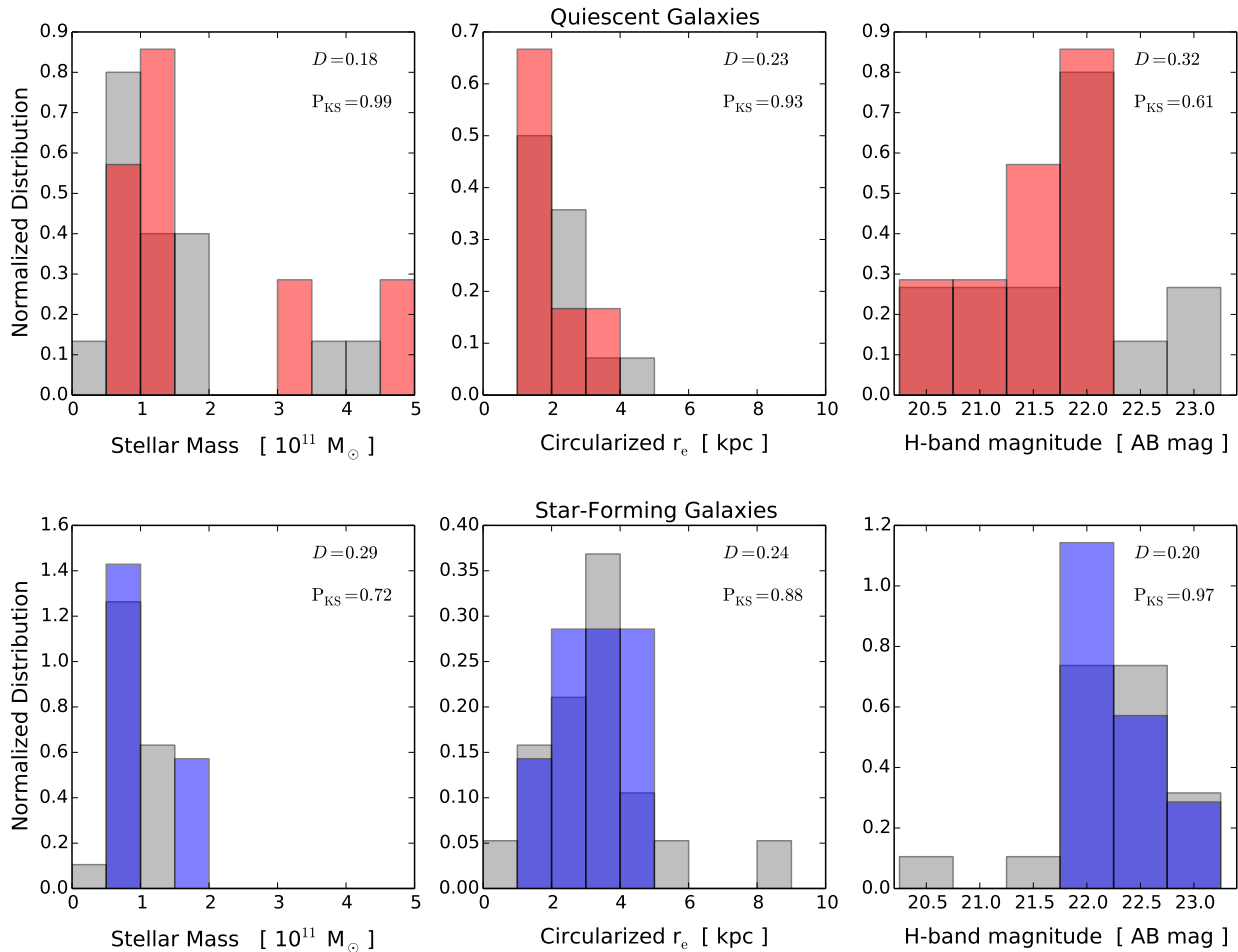


Figure 1. Normalized distributions of stellar mass, effective radii, and H -band AB magnitudes. In each panel, the underlying gray histogram shows the full photometric parent sample of quiescent galaxies, which was selected from the mass-complete catalog. The red histogram shows the spectroscopic sub-sample. In the corner of each panel, we show the KS statistic, D , and the p -value, P_{KS} . The top row shows the quiescent galaxies and the lower row shows the star-forming galaxies.

tion along with the photometry. Before fitting the spectra, we binned them by a factor of 8. We did this to avoid being affected by differences in the resolution of the models and the actual spectra. Some of this difference was caused by morphological broadening which arises due to the fact that we are using slitless spectroscopy on extended objects. We chose to re-bin the spectra as this is much faster than having to match entire grid of templates in the fit to the resolution and sampling of the grism spectra, especially since the resolution is different for each source. The addition of spectral information improved the parameter estimation. However, the strong re-binning of the spectra made the improvement on the redshift very limited. We therefore used the spectral fits to improve the redshifts by comparing the best-fit template to the original spectrum before the re-binning. We cross-correlated the two to obtain a higher precision on the best-fit redshift. Before comparing the spectra and templates we match the resolution and sampling of the templates to those of the spectra. For spectra with low SNR we re-binned the spectra by a factor of 2 or 4 until we reached a SNR per pixel of at least 4. The uncertainty on the redshift is thus mainly determined by the spectral re-binning. Figure 2 shows the individual spec-

tra and SEDs along with their best fitting template for the spectroscopic sample. All the parameters from the SED fits are summarized in Table 2 where we also list the strength of the 4000 Å break for comparison with other studies. These are calculated using the original definition from Bruzual A. (1983).

To estimate the improvement on the stellar mass with the higher precision on redshifts, we performed a last fit to the spectroscopic subsample while keeping the redshifts fixed to the spectrophotometric redshifts determined above. We note that this approach slightly underestimates the uncertainties on the masses, however, we were not able to propagate the redshift uncertainties directly using the FAST code. Instead, we performed two further fits, this time using the upper and lower 1σ limits on the spectro-photometric redshifts. The effect of varying the redshift this way did in most cases not lead to any significant change. In Fig. 3, we show the individual mass estimates from the best-fit and the effect on the mass determination by using the upper and lower boundaries on the redshift. For all sources the variations are within the 1σ limits from the fixed-redshift fits. We therefore neglect the effect from the redshift uncertainties on the stellar mass estimates.

Table 1

Description of the full sample. The galaxy type refers to the UVJ classification as either star-forming (SFG) or quiescent (QG).

Catalog ID	Grism ID	RA (deg)	DEC (deg)	z_{phot}	H_{160} (AB mag)	Type
118543	ibhm42.014	150.1039700	2.1864245	$2.09^{+0.12}_{-0.12}$	22.50 ± 0.10	SFG
119753		150.1430800	2.2003083	$1.99^{+0.17}_{-0.16}$	22.00 ± 0.09	QG
121761	ibhm42.243	150.1172600	2.2238793	$1.97^{+0.11}_{-0.10}$	21.96 ± 0.05	SFG
122398	ibhm30.211	150.1539200	2.2323158	$1.95^{+0.10}_{-0.09}$	21.84 ± 0.05	QG
123235	ibhm41.170	150.0981300	2.2428155	$2.01^{+0.21}_{-0.20}$	22.85 ± 0.13	SFG
123324		150.0905500	2.2441640	$2.26^{+0.11}_{-0.12}$	22.54 ± 0.12	SFG
123780		150.0768000	2.2492609	$2.26^{+0.20}_{-0.20}$	22.42 ± 0.18	SFG
123817		150.0765800	2.2496693	$2.13^{+0.13}_{-0.13}$	22.36 ± 0.11	SFG
124168		150.1064100	2.2515926	$2.04^{+0.08}_{-0.10}$	22.65 ± 0.13	SFG
124666	ibhm33.161	150.0656400	2.2609785	$1.98^{+0.10}_{-0.11}$	21.04 ± 0.04	QG
124686		150.0639300	2.2611351	$2.11^{+0.17}_{-0.13}$	21.95 ± 0.06	QG
126073		150.1429400	2.2785251	$2.21^{+0.11}_{-0.09}$	22.15 ± 0.07	QG
126301		150.0778700	2.2811451	$2.05^{+0.11}_{-0.11}$	22.10 ± 0.07	SFG
126824	ibhm40.143	150.1213500	2.2851899	$2.19^{+0.13}_{-0.13}$	22.06 ± 0.09	SFG
126952		150.0705900	2.2892091	$2.28^{+0.27}_{-0.29}$	23.21 ± 0.22	SFG
127466	ibhm51.200	150.1553000	2.2948477	$1.97^{+0.14}_{-0.12}$	22.01 ± 0.07	QG
127603	ibhm51.292	150.1593200	2.2968187	$1.96^{+0.19}_{-0.17}$	22.60 ± 0.11	SFG
127617		150.1196100	2.2958610	$2.07^{+0.07}_{-0.07}$	20.73 ± 0.02	SFG
128061	ibhm54.240	150.0739400	2.2979755	$2.09^{+0.02}_{-0.02}$	20.44 ± 0.02	QG
128093	ibhm54.256	150.0746200	2.3020012	$2.18^{+0.10}_{-0.09}$	21.87 ± 0.05	SFG
128977		150.1122100	2.3140118	$2.23^{+0.20}_{-0.21}$	23.23 ± 0.21	SFG
129022	ibhm52.157	150.0961200	2.3134823	$2.05^{+0.12}_{-0.11}$	21.47 ± 0.04	QG
132654		150.0918400	2.3567889	$1.97^{+0.22}_{-0.21}$	23.04 ± 0.14	QG
133784		150.1292900	2.3695824	$2.03^{+0.22}_{-0.24}$	22.84 ± 0.13	QG
133915		150.1335800	2.3703971	$1.86^{+0.12}_{-0.12}$	21.58 ± 0.05	SFG
134068	ibhm46.116	150.1635700	2.3724642	$2.02^{+0.10}_{-0.09}$	21.89 ± 0.06	SFG
134172		150.1102600	2.3741243	$2.26^{+0.21}_{-0.22}$	22.53 ± 0.12	QG
135214		150.1841100	2.3863766	$1.89^{+0.10}_{-0.10}$	22.23 ± 0.08	SFG
135878	ibhm53.253	150.1085100	2.3938241	$1.94^{+0.09}_{-0.08}$	21.33 ± 0.04	QG
139823		150.1546300	2.4443281	$1.87^{+0.08}_{-0.08}$	20.69 ± 0.02	QG
140122	ibhm35.195	150.0796800	2.4495835	$2.16^{+0.15}_{-0.17}$	21.88 ± 0.05	QG
204878		150.1114000	2.4530017	$2.07^{+0.14}_{-0.12}$	22.48 ± 0.10	SFG
207084		150.1361200	2.4815121	$2.05^{+0.14}_{-0.14}$	21.97 ± 0.07	SFG
207144		150.1395000	2.4818728	$1.91^{+0.13}_{-0.11}$	21.00 ± 0.04	QG

In the previous section, we described the *UVJ* method we use to select quiescent galaxies. Now with the stellar population parameters we can investigate the relation between the classification from the *UVJ* criteria and the inferred star formation rates. When looking at the specific star formation rate (sSFR \equiv SFR/ M_*), we find a strong correlation between the classification of quiescent galaxies from the *UVJ* method and galaxies with sSFR $< -10.5 \text{ yr}^{-1}$. There are only two star-forming galaxies (from *UVJ* criteria) below this cut-off, and one quiescent galaxy above it. For the spectroscopic sample, only one star-forming galaxy lies below the sSFR limit of -10.5 yr^{-1} .

Lastly, we use the inferred ages and redshifts for the spectroscopic sample to compute formation redshifts. In Fig. 4, we show the distribution of formation redshifts for the full sample as well as for the spectroscopic sub-sample of quiescent galaxies.

5. STRUCTURAL FITTING

When possible we use the tabulated values from van der Wel et al. (2012). In cases of bad fits (flag values 1, 2 and 3 in their table), we redid the fits ourselves in order to improve the fit. For this purpose, we used the same point spread functions as were used by van der Wel et al. (private communication). See below for individual comments on the sources where a standard Sérsic fit was not adequate. All neighbouring objects were included in the modelling as either individual Sérsic components or point sources. In three cases (#124666, #128093, and #207144), the fits did not converge immediately and we therefore kept the magnitude fixed to the value obtained from the CANDELS catalog. This way we were able to get the fit to converge.

For the target #127466, we were not able to get a good fit with a Sérsic component due to the source being very compact. The target is furthermore surrounded by a few companions and a very spatially extended low surface brightness component. This makes it hard to separate the various components and estimate the actual background, which caused the divergent behaviour of GALFIT. Instead we tried to estimate the size using a curve-of-growth approach. We use circular apertures to infer the effective radius since the source has very low ellipticity (minor-to-major axis ratio is 0.98). This results in a size estimate of $r_e = 0.22 \pm 0.01$ arcsec.

Finally, we note that the target #133915 resides in a very dense area with many compact neighbours, the size may therefore be slightly overestimated.

All the inferred sizes are included in Table 3 as circularized half-light radii (r_e) in kpc. Throughout the rest of the paper, circularized radii will be used. We use the minor-to-major axis ratio, q , from the GALFIT analysis to calculate the circularized radii: $r_e = a_e \sqrt{q}$. The details (models and residuals) of the analysis are shown in appendix B.

6. THE MASS-SIZE RELATION

We have used our sample of spectroscopically confirmed galaxies at redshift $z \approx 2$ to investigate the mass-size relation of quiescent galaxies at high redshift. We parameterize the relation following Newman et al. (2012) and others:

$$r_e = \gamma \left(\frac{M_*}{10^{11} M_\odot} \right)^\beta = \gamma M_{11}^\beta. \quad (1)$$

We fit the relation in log-log space using the errors on both the stellar masses and sizes, hence we wish to minimize the perpendicular distance from the line to each point and not simply the vertical distance. This can be expressed in terms of the likelihood estimator, assuming Gaussian uncertainties:

$$\ln(L) = - \sum \frac{\Delta_i^2}{2(\sigma_i^2 + V)} - \frac{1}{2} \sum (\sigma_i^2 + V), \quad (2)$$

where

$$\Delta_i = (y_i - \beta x_i - b) / \sqrt{1 + \beta^2} \text{ and } \sigma_i^2 = \sigma_{y_i}^2 + \beta^2 \sigma_{x_i}^2.$$

Δ_i here denotes the orthogonal distance from the datapoint (x_i, y_i) to the line, and σ_i^2 denotes the projected variance for each datapoint taking into account the errors on stellar mass and size. In this notation x refers to $\log(M_*/10^{11} M_\odot)$ and y refers to $\log(r_e/\text{kpc})$. The V that enters in the likelihood refers to the intrinsic (Gaussian) variance perpendicular to the line, which also is a free parameter in the fit. We fit the relation to the data using a Bayesian approach to estimate the parameters and their confidence intervals. We use flat priors on all parameters: $-10 < \beta < 10$, $-2 < b < 2$, and $-10 < \ln(V) < 1$.

Firstly, we fit the quiescent galaxies using only the photometric data. Hereafter we include the spectroscopic data to investigate the improvement. All the fit values are summarized in Table 4. The scatter we infer from the fit is the scatter perpendicular to the line, however, the quantity we are interested in is the scatter in the sizes. We thus transform the scatter to the vertical scatter as follows: $\sigma_{\log r_e}^2 = V(1 + \beta^2)$.

The addition of spectroscopic information significantly improves the estimate of the scatter since the large uncertainty on the photometric masses leads to an underestimation of the scatter. The mass-normalized size (γ) remains almost unaffected. In the rest of the paper, we will refer to the fit obtained using the spectroscopic data combined with the full photometric sample of quiescent galaxies. The slope is poorly constrained due to the low number of data points and the large uncertainty on the stellar masses, thus still consistent with what is found by Newman et al. (2012) at similar redshifts. Recently, van der Wel et al. (2014) studied the evolution of size, slope and scatter from redshift $z \sim 2$, however, they use the effective semi-major axis and not circularized radii as in previous studies. Therefore, their results on slope and scatter cannot be directly compared to the parameters obtained in this analysis.

In Fig. 5, we show the mass-size relation for the sample of quiescent galaxies with and without spectra as red squares and triangles, respectively. We compare our data to local early type galaxies with kinematical data from ATLAS^{3D} (Cappellari et al. 2011). In order to compare our high redshift sample to the that of the ATLAS^{3D}-team we fit the power-law relation given above to their data using the same mass-limit as for our data. From the best fit to the ATLAS^{3D} sample, we find the following slope of $\beta_0 = 0.68 \pm 0.06$, a mass-

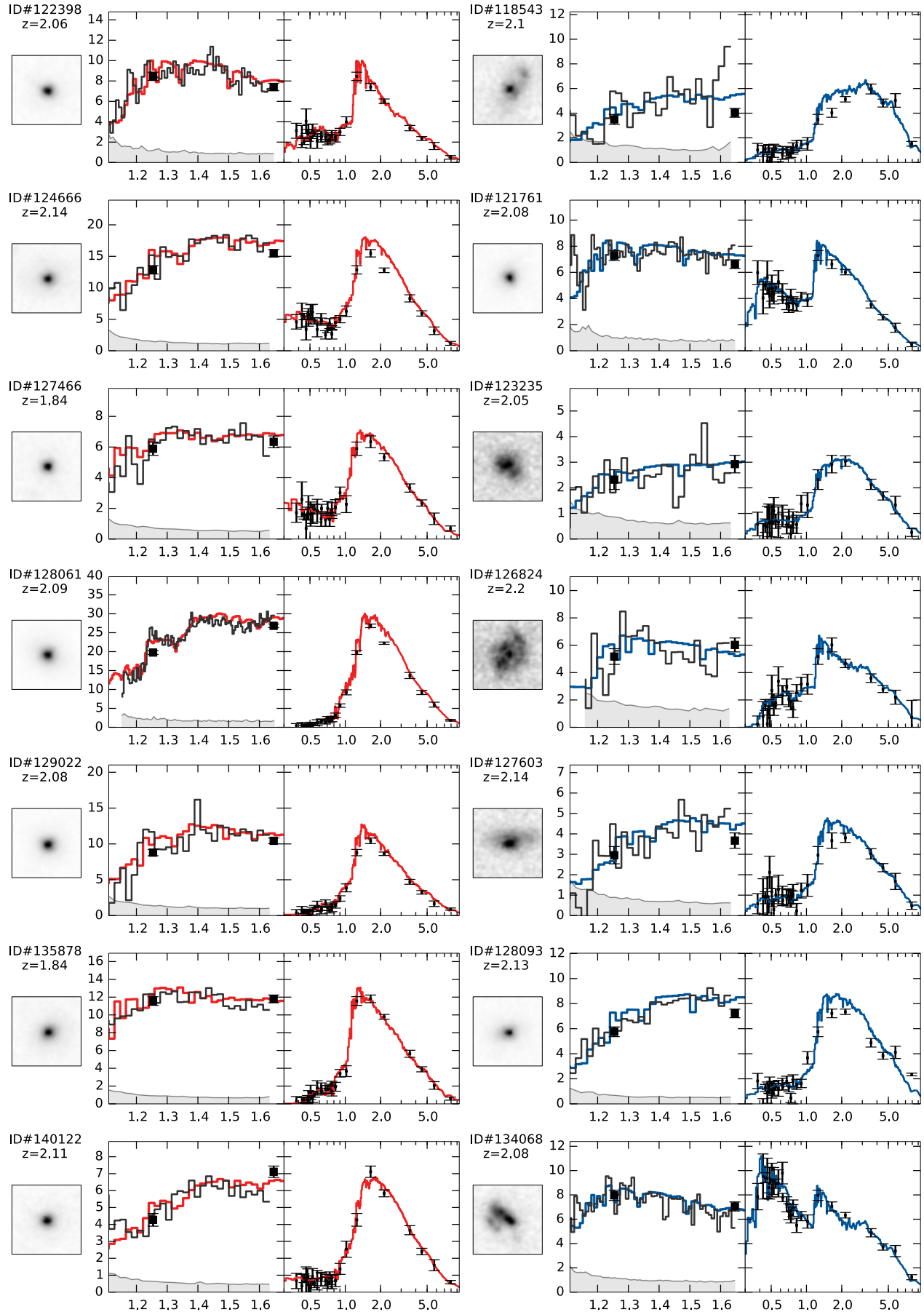


Figure 2. (left) 2.4×2.4 arcsec² H_{160} -band image, (middle) 1D extracted grism spectrum in black and error spectrum in grey, and (right) photometric SED. Both the middle and right panels show wavelength in units of μm vs. f_λ in units of $10^{-19} \text{ erg}^{-1} \text{ s}^{-1} \text{ cm}^{-2} \text{ \AA}^{-1}$. The colored line shows the best-fit model from FAST convolved and rebinned to match the resolution of the grism spectra. Quiescent (star-forming) galaxies are shown in the left (right) column in red (blue).

Table 2

Parameters from SED fitting. The upper part (above the line) shows the fits with spectral data available. The redshift is in this case the spectro-photometric redshift, see text. The lower part shows the photometric sample, where z here refers to the photometric redshift.

ID	z	$\log(M_*)$ (M_\odot)	$\log(\text{Age})$ (yr)	$\log(Z/Z_\odot)$	A_V (mag)	$\log(\text{SSFR})$ (yr^{-1})	$\log(\tau)$ (yr)	D(4000)
118543	2.10 ± 0.05	$11.20^{+0.04}_{-0.05}$	$8.80^{+0.20}_{-0.19}$	$0.050^{+0.000}_{-0.014}$	$1.80^{+0.20}_{-0.30}$	$-9.72^{+0.26}_{-0.19}$	$8.20^{+0.20}_{-0.19}$	3.05 ± 1.76
121761	2.08 ± 0.02	$10.87^{+0.09}_{-0.18}$	$8.80^{+0.30}_{-0.57}$	$0.004^{+0.015}_{-0.000}$	$1.30^{+0.27}_{-0.43}$	$-9.26^{+0.27}_{-0.39}$	$8.40^{+0.36}_{-0.75}$	1.09 ± 0.10
122398	2.06 ± 0.02	$10.76^{+0.05}_{-0.05}$	$8.80^{+0.19}_{-0.16}$	$0.050^{+0.000}_{-0.040}$	$0.20^{+0.36}_{-0.20}$	$-10.53^{+0.09}_{-0.10}$	$8.00^{+0.19}_{-0.16}$	1.30 ± 0.13
123235	2.05 ± 0.10	$10.79^{+0.20}_{-0.21}$	$9.10^{+0.40}_{-0.78}$	$0.004^{+0.036}_{-0.000}$	$1.60^{+0.40}_{-0.62}$	$-9.74^{+0.55}_{-1.02}$	$8.60^{+0.51}_{-1.18}$	1.59 ± 0.68
124666	2.14 ± 0.05	$11.49^{+0.00}_{-0.29}$	$9.40^{+0.00}_{-0.42}$	$0.004^{+0.046}_{-0.000}$	$0.50^{+0.21}_{-0.50}$	$-10.62^{+0.36}_{-0.38}$	$8.70^{+0.01}_{-0.52}$	1.30 ± 0.13
126824	2.20 ± 0.02	$10.78^{+0.11}_{-0.05}$	$8.10^{+0.19}_{-0.12}$	$0.050^{+0.000}_{-0.031}$	$1.50^{+0.32}_{-0.20}$	$-11.26^{+1.38}_{-1.09}$	$7.10^{+0.38}_{-0.10}$	1.67 ± 0.44
127466	1.84 ± 0.05	$10.84^{+0.14}_{-0.07}$	$9.30^{+0.20}_{-0.24}$	$0.008^{+0.019}_{-0.004}$	$0.50^{+0.28}_{-0.11}$	$-10.53^{+0.18}_{-0.18}$	$8.60^{+0.23}_{-0.24}$	1.34 ± 0.35
127603	2.14 ± 0.05	$10.95^{+0.13}_{-0.13}$	$9.10^{+0.30}_{-0.61}$	$0.020^{+0.030}_{-0.016}$	$0.90^{+0.96}_{-0.21}$	$-10.35^{+0.54}_{-0.50}$	$8.40^{+0.33}_{-0.81}$	1.19 ± 0.30
128061	2.09 ± 0.01	$11.68^{+0.11}_{-0.10}$	$9.40^{+0.10}_{-0.40}$	$0.008^{+0.015}_{-0.004}$	$0.10^{+0.42}_{-0.10}$	< -12.28	$8.20^{+0.30}_{-1.20}$	1.73 ± 0.10
128093	2.13 ± 0.05	$11.28^{+0.11}_{-0.18}$	$9.00^{+0.40}_{-0.07}$	$0.020^{+0.030}_{-0.016}$	$1.20^{+0.15}_{-0.75}$	$-10.26^{+0.00}_{-0.46}$	$8.30^{+0.40}_{-0.15}$	1.28 ± 0.13
129022	2.08 ± 0.05	$11.11^{+0.01}_{-0.10}$	$9.00^{+0.12}_{-0.09}$	$0.020^{+0.012}_{-0.004}$	$0.40^{+0.09}_{-0.40}$	< -12.10	$8.00^{+0.12}_{-1.00}$	1.86 ± 0.36
134068	2.08 ± 0.02	$10.84^{+0.11}_{-0.15}$	$8.90^{+0.23}_{-0.46}$	$0.050^{+0.000}_{-0.016}$	$1.30^{+0.22}_{-0.17}$	$-8.74^{+0.30}_{-0.21}$	$9.90^{+0.00}_{-1.45}$	1.11 ± 0.10
135878	1.84 ± 0.10	$11.02^{+0.04}_{-0.04}$	$8.90^{+0.06}_{-0.14}$	$0.020^{+0.009}_{-0.007}$	$0.70^{+0.30}_{-0.12}$	< -12.01	$7.80^{+0.17}_{-0.80}$	1.04 ± 0.15
140122	2.11 ± 0.10	$11.15^{+0.05}_{-0.13}$	$9.50^{+0.00}_{-0.38}$	$0.004^{+0.039}_{-0.000}$	$0.50^{+0.21}_{-0.50}$	$-11.17^{+0.27}_{-0.60}$	$8.70^{+0.02}_{-0.36}$	1.40 ± 0.19
119753	$1.99^{+0.17}_{-0.16}$	$11.24^{+0.17}_{-0.34}$	$9.45^{+0.15}_{-0.62}$	$0.008^{+0.042}_{-0.004}$	$1.00^{+1.27}_{-1.00}$	$-10.44^{+1.16}_{-0.78}$	$8.80^{+1.10}_{-0.68}$	
123324	$2.26^{+0.11}_{-0.12}$	$10.62^{+0.31}_{-0.45}$	$8.80^{+0.80}_{-1.18}$	$0.050^{+0.000}_{-0.046}$	$1.80^{+0.70}_{-0.53}$	$-9.12^{+0.88}_{-0.54}$	$8.50^{+1.40}_{-1.50}$	
123780	$2.26^{+0.20}_{-0.20}$	$10.80^{+0.32}_{-0.59}$	$9.00^{+0.60}_{-1.29}$	$0.004^{+0.046}_{-0.000}$	$1.60^{+0.90}_{-1.46}$	< -7.86	$8.80^{+1.10}_{-1.80}$	
123817	$2.13^{+0.13}_{-0.13}$	$10.98^{+0.12}_{-0.33}$	$9.50^{+0.10}_{-0.60}$	$0.004^{+0.046}_{-0.000}$	$1.00^{+0.64}_{-0.59}$	$-9.64^{+0.78}_{-0.43}$	$9.30^{+0.60}_{-0.89}$	
124168	$2.04^{+0.08}_{-0.10}$	$11.16^{+0.30}_{-0.32}$	$9.55^{+0.05}_{-0.96}$	$0.050^{+0.000}_{-0.041}$	$2.20^{+0.30}_{-0.78}$	$-9.52^{+0.60}_{-0.64}$	$9.60^{+0.30}_{-1.41}$	
124686	$2.11^{+0.17}_{-0.13}$	$10.96^{+0.23}_{-0.27}$	$9.20^{+0.40}_{-0.71}$	$0.004^{+0.041}_{-0.000}$	$0.50^{+1.52}_{-0.50}$	< -9.91	$8.30^{+0.70}_{-1.30}$	
126073	$2.21^{+0.11}_{-0.09}$	$10.67^{+0.35}_{-0.07}$	$9.10^{+0.37}_{-0.42}$	$0.008^{+0.042}_{-0.004}$	$0.00^{+0.73}_{-0.00}$	< -11.32	$7.60^{+0.93}_{-0.60}$	
126301	$2.05^{+0.11}_{-0.11}$	$11.11^{+0.27}_{-0.17}$	$9.20^{+0.40}_{-0.37}$	$0.050^{+0.000}_{-0.045}$	$1.20^{+0.96}_{-0.42}$	$-10.09^{+0.71}_{-0.44}$	$8.60^{+1.12}_{-0.35}$	
126952	$2.28^{+0.27}_{-0.29}$	$10.70^{+0.51}_{-0.37}$	$8.35^{+1.25}_{-0.37}$	$0.004^{+0.046}_{-0.000}$	$2.50^{+0.00}_{-2.01}$	< -8.97	$7.30^{+2.60}_{-0.30}$	
127617	$2.07^{+0.07}_{-0.07}$	$11.14^{+0.22}_{-0.14}$	$8.40^{+0.62}_{-0.50}$	$0.008^{+0.030}_{-0.004}$	$1.80^{+0.27}_{-0.47}$	$-8.90^{+0.37}_{-3.36}$	$8.00^{+1.90}_{-1.00}$	
128977	$2.23^{+0.20}_{-0.21}$	$11.03^{+0.27}_{-0.59}$	$9.50^{+0.10}_{-1.72}$	$0.020^{+0.030}_{-0.016}$	$1.90^{+0.60}_{-1.31}$	$-9.57^{+1.03}_{-2.69}$	$9.40^{+0.50}_{-2.40}$	
132654	$1.97^{+0.22}_{-0.21}$	$10.81^{+0.21}_{-0.50}$	$9.55^{+0.05}_{-1.26}$	$0.004^{+0.046}_{-0.000}$	$1.50^{+1.00}_{-1.50}$	< -9.82	$8.90^{+1.00}_{-1.90}$	
133784	$2.03^{+0.22}_{-0.24}$	$10.86^{+0.25}_{-0.45}$	$9.25^{+0.35}_{-0.99}$	$0.004^{+0.046}_{-0.000}$	$1.20^{+1.30}_{-1.07}$	< -9.39	$8.40^{+0.86}_{-1.40}$	
133915	$1.86^{+0.12}_{-0.12}$	$10.87^{+0.18}_{-0.25}$	$9.10^{+0.50}_{-0.79}$	$0.008^{+0.034}_{-0.004}$	$1.00^{+0.73}_{-0.44}$	$-9.54^{+0.81}_{-0.34}$	$8.70^{+1.20}_{-0.97}$	
134172	$2.26^{+0.21}_{-0.22}$	$11.13^{+0.09}_{-0.42}$	$9.45^{+0.11}_{-0.63}$	$0.004^{+0.046}_{-0.000}$	$0.70^{+0.87}_{-0.70}$	< -10.62	$8.60^{+0.27}_{-1.60}$	
135214	$1.89^{+0.10}_{-0.10}$	$10.71^{+0.18}_{-0.17}$	$8.85^{+0.54}_{-0.47}$	$0.050^{+0.000}_{-0.030}$	$1.30^{+0.37}_{-0.46}$	$-9.22^{+0.38}_{-0.37}$	$8.50^{+1.40}_{-0.58}$	
139823	$1.87^{+0.08}_{-0.08}$	$11.19^{+0.29}_{-0.06}$	$9.20^{+0.26}_{-0.20}$	$0.008^{+0.017}_{-0.004}$	$0.20^{+0.49}_{-0.20}$	$-11.50^{+0.29}_{-0.94}$	$8.30^{+0.31}_{-0.29}$	
204878	$2.07^{+0.14}_{-0.12}$	$10.95^{+0.41}_{-0.24}$	$9.15^{+0.45}_{-0.93}$	$0.008^{+0.042}_{-0.004}$	$2.50^{+0.00}_{-1.53}$	< -9.36	$8.70^{+1.20}_{-1.70}$	
207084	$2.05^{+0.14}_{-0.14}$	$10.75^{+0.25}_{-0.27}$	$8.90^{+0.70}_{-1.04}$	$0.004^{+0.040}_{-0.000}$	$1.70^{+0.45}_{-0.92}$	$-8.95^{+0.60}_{-3.31}$	$8.90^{+1.00}_{-1.90}$	
207144	$1.91^{+0.13}_{-0.11}$	$11.62^{+0.07}_{-0.32}$	$9.50^{+0.09}_{-0.51}$	$0.020^{+0.030}_{-0.016}$	$0.10^{+1.37}_{-0.10}$	$-11.78^{+1.07}_{-0.16}$	$8.60^{+0.28}_{-0.55}$	

Table 3
Morphological Parameters from GALFIT. The top part of the table (above the horizontal line) shows the spectroscopic sample. Below the line is the rest of the photometric sample.

ID	r_e (kpc)	Sérsic n	b/a	Ref.
118543	4.41 ± 0.39	2.57 ± 0.30	0.51 ± 0.03	2
121761	1.19 ± 0.04	4.66 ± 0.29	0.87 ± 0.02	2
122398	1.59 ± 0.05	6.30 ± 0.36	0.70 ± 0.02	2
123235	2.78 ± 0.11	0.72 ± 0.10	0.74 ± 0.02	2
124666*	10.00 ± 0.10	9.88 ± 0.08	0.69 ± 0.01	1
126824	4.39 ± 0.13	0.53 ± 0.07	0.74 ± 0.02	2
127466	1.84 ± 0.10	...	0.98 ± 0.03	1, 2
127603	3.05 ± 0.15	1.37 ± 0.13	0.48 ± 0.02	2
128061	2.58 ± 0.05	4.69 ± 0.17	0.82 ± 0.01	2
128093*	3.04 ± 0.15	8.53 ± 0.98	0.53 ± 0.04	1
129022	1.34 ± 0.03	3.02 ± 0.14	0.87 ± 0.02	2
134068	2.85 ± 0.03	0.57 ± 0.02	0.58 ± 0.01	2
135878	3.42 ± 0.20	5.27 ± 0.23	0.78 ± 0.02	1
140122	1.67 ± 0.09	4.92 ± 0.50	0.79 ± 0.04	2
<hr/>				
119753	2.57 ± 0.17	0.99 ± 0.18	0.36 ± 0.03	2
123324	2.16 ± 0.34	3.61 ± 0.63	0.39 ± 0.04	1
123780	1.73 ± 0.17	1.41 ± 0.35	0.55 ± 0.06	2
123817	3.10 ± 0.16	4.61 ± 0.19	0.85 ± 0.02	1
124168	3.33 ± 0.55	2.46 ± 0.58	0.68 ± 0.05	2
124686	1.51 ± 0.05	5.65 ± 0.21	0.74 ± 0.01	1
126073	1.58 ± 0.09	5.43 ± 0.36	0.86 ± 0.02	1
126301	5.67 ± 0.46	4.18 ± 0.20	0.81 ± 0.02	1
126952	3.35 ± 0.24	0.44 ± 0.14	0.43 ± 0.04	2
127617	0.46 ± 0.01	8.00 ± 0.63	0.67 ± 0.03	2
128977	3.36 ± 0.14	0.50 ± 0.08	0.28 ± 0.02	2
132654	2.49 ± 0.13	1.46 ± 0.15	0.42 ± 0.02	2
133784	2.12 ± 0.08	0.77 ± 0.09	0.51 ± 0.02	2
133915	8.75 ± 0.46	5.60 ± 0.14	0.70 ± 0.01	1
134172	2.54 ± 0.40	5.11 ± 1.07	0.84 ± 0.06	2
135214	2.76 ± 0.05	0.64 ± 0.04	0.39 ± 0.01	2
139823	1.37 ± 0.02	4.65 ± 0.15	0.44 ± 0.01	2
204878	3.33 ± 0.32	1.70 ± 0.26	0.46 ± 0.04	2
207084	1.25 ± 0.04	3.08 ± 0.19	0.53 ± 0.02	2
207144*	2.88 ± 0.06	2.25 ± 0.08	0.77 ± 0.02	1

References: (1) This work; (2) van der Wel et al. (2012).

* Sources where the magnitude was kept fixed, see text.

Table 4

Parameter estimates for mass–size relation of quiescent galaxies at $z \sim 2$ with and without spectral data.

	β	$\log(\gamma/\text{kpc})$	$\sigma_{\log r_e}$
Photometry	0.82 ± 0.22	$0.30^{+0.07}_{-0.08}$	$0.05^{+0.09}_{-0.04}$
Phot. + spectra	$0.53^{+0.29}_{-0.21}$	0.29 ± 0.07	$0.17^{+0.05}_{-0.04}$

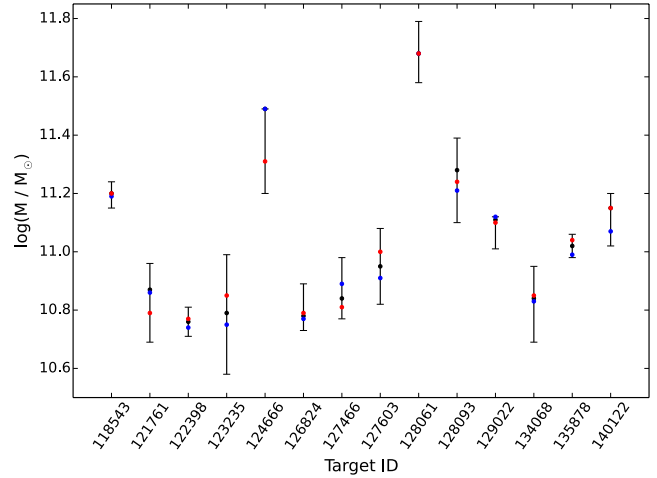


Figure 3. Effects of varying spectro-photometric redshift in the SED fits from FAST. The black points with errorbars show the best-fit stellar mass and 68% confidence intervals with the assumed redshift for each target. The effect on stellar mass when using the upper and lower boundaries on the redshifts is shown by the red and blue points, respectively.

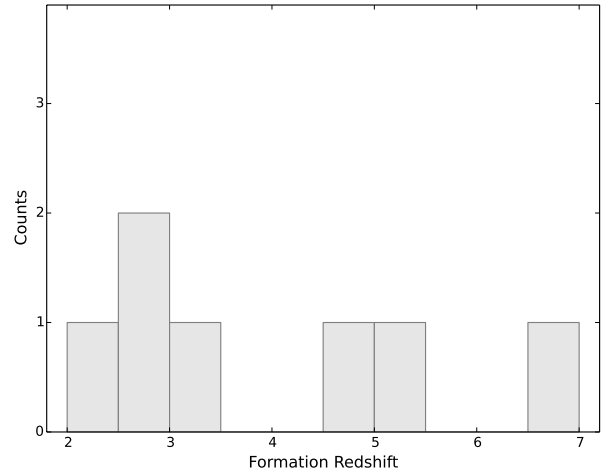


Figure 4. Distribution of formation redshifts for the quiescent galaxies. The gray distribution shows the full photometric and spectroscopic sample. The red distribution is the spectroscopic sub-sample only. Due to the much larger uncertainties on both redshift and stellar age for the photometric sample, these formation redshifts should only be considered indicative.

normalized size of $\log(\gamma_0/\text{kpc}) = 0.59 \pm 0.03$, and a scatter of $\sigma_0 = 0.13 \pm 0.01$. For this analysis, we have used the tabulated values from Cappellari et al. (2013). Specifically, we note that we used the $\log(r_{1/2})$ to infer the sizes. The inferred slope for the local relation is significantly steeper than the value found by Shen et al. (2003) ($\beta_{z=0} = 0.56$). Guo et al. (2009) find a slightly higher value for the slope of $\beta_{z=0} = 0.70 \pm 0.05$ which is in very good agreement with the result from the ATLAS^{3D} data.

It is clearly visible that the quiescent galaxies from this work are smaller than local quiescent galaxies at the same mass. Moreover, the figure shows that the various samples of local galaxies infer slightly different normalizations and slopes of the relation. The slope derived from the ATLAS^{3D} data is in very good agreement with the slope derived by Guo et al. (2009). On the other

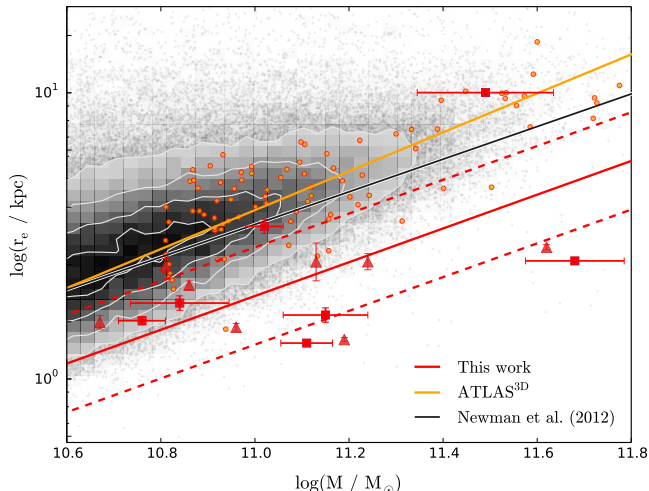


Figure 5. Mass-size relation using circularized effective radii for quiescent galaxies. The galaxies at high redshift (red points and red line) are smaller than the local relation inferred from ATLAS^{3D} data (orange points and solid line). For comparison, we show the local relation from Newman et al. (2012) as the black line. Local data from SDSS quiescent galaxies with Sérsic indices larger than $n > 2.5$ (following Shen et al. (2003)) are shown as the underlying distribution in gray. The red squares with error bars on both mass and size indicate the spectroscopic sample. The sample with only photometry available is shown as red triangles. Here we do not show the uncertainties on the mass estimates, but they are typically of the order $\sim 0.2 - 0.3$ dex, the uncertainties are listed in Table 2 for reference.

hand, the relation derived by Newman et al. (2012) and Shen et al. (2003) is much shallower. These differences are most likely caused by the different fitting techniques as well as the different approaches used to separate quiescent and star-forming galaxies. The scatter inferred for the relation locally is found to be $\sigma_0 = 0.16$ by Newman et al. (2012) using SDSS data, this is in good agreement with, though slightly larger than, the scatter inferred from the ATLAS^{3D} data. Given the value we infer at high redshift, $\sigma = 0.17^{+0.05}_{-0.04}$, this indicates that the scatter remains constant with redshift.

Although we cannot compare our values directly with the van der Wel et al. (2014) study, we can still compare to their evolutionary trends. They find no evidence for evolution in scatter and slope with time, consistent with the results presented here.

6.1. Size Evolution

We now take a closer look at the offset towards smaller sizes visible in Fig. 5 between our sample at high redshift and the local sample. This offset has been studied in great detail (e.g., Daddi et al. 2005; Trujillo et al. 2006; Toft et al. 2007; Zirm et al. 2007; Buitrago et al. 2008; van Dokkum et al. 2008; Damjanov et al. 2011; Bruce et al. 2012; Newman et al. 2012) and various explanations have been put forward to explain the required evolution in sizes, e.g., merging or feedback from quasars (Fan, Lapi, De Zotti, & Danese 2008). We here investigate a simple scenario in which the individual galaxies themselves do not need to increase significantly in size, but rather that the average of the population as a whole increases (e.g., Cassata et al. 2011; Trujillo et al. 2012; Carollo et al. 2013; Poggianti et al. 2013). We use our measurements of sizes and scatter at high redshift in combinations with those from Newman et al. (2012) to motivate the initial

values for the size evolution.

Newman et al. (2012) study the size evolution of massive galaxies both star-forming and quiescent and find that the star-forming galaxies on average are a factor of 2 larger than the quiescent population at all times above redshift $z > 0.5$. This is consistent with the fact that the star-forming galaxies in our sample on average are a factor of 1.8 larger than the quiescent galaxies at a fixed mass ($10^{11} M_\odot$). The evolution of the mean size of quiescent galaxies might then simply be driven by the addition of larger, newly quenched galaxies at lower redshifts to the already quenched population. Carollo et al. (2013) recently showed that the evolution of the sizes of passively evolving galaxies at $z < 1$ is driven by this "dilution" of the compact population. In order to test this picture and evaluate the effect on the scatter in sizes, we have taken the measured sizes normalized to a stellar mass of $10^{11} M_\odot$ from Newman et al. (2012) at redshift $2.0 < z < 2.5$ and generated an initial population of quiescent (QG) and star-forming (SFG) galaxies taking into account the observed number densities at that redshift for galaxies with comparable masses from Brammer et al. (2011). We have shifted the data from Newman et al. from a Salpeter IMF to the assumed Chabrier IMF in this work. The distribution of sizes for the populations are drawn from a log-normal distribution with an average size initially dictated by the observations for QGs while for SFGs we simply use the fact that star-forming galaxies on average are twice as big. The distribution of QGs is assumed to have a scatter of 0.17 dex initially, motivated by the findings in this work. The study by van der Wel et al. (2014) show that the scatter of star-forming galaxies remains constant with redshift and that the scatter is roughly 0.5 dex larger than that of quiescent galaxies. We therefore use a value of 0.22 for the scatter of SFGs in our model. We note that the chosen value for the initial scatter of SFGs does not change the conclusions of the model, it only enhances the increase in the modelled evolution of the scatter.

We then simply assume that the SFGs at the given redshift will be quenched after a fixed time, t_{quench} , and add them to the already existing population of quiescent galaxies. For each time-step, we generate a new population of SFGs with a mean size that is twice as big as the mean size of the quiescent galaxies already in place, and after another t_{quench} these will be added to the quiescent population. The generated number of SFGs varies according to the observed number density of SFGs. We have assumed that the scatter of the SFG population is constant with time and that no galaxy-galaxy interactions occur, i.e., no new massive galaxies form by merging of lower-mass galaxies. Furthermore, we assume that galaxies maintain their sizes after they have been quenched and that no further star formation occurs once the galaxies have been quenched. We run this model three times for various quenching time-scales, t_{quench} : 1.0, 1.2, and 1.5 Gyr. These time scales are consistent with the results of Bedregal et al. (2013).

The results of this simple model are shown in Fig. 6. The top panel shows the evolution in number density. The red and blue points are data from Brammer et al. (2011) for quiescent and star-forming galaxies, respectively. The black and grey points show the modeled evolution in the number density assuming different quench-

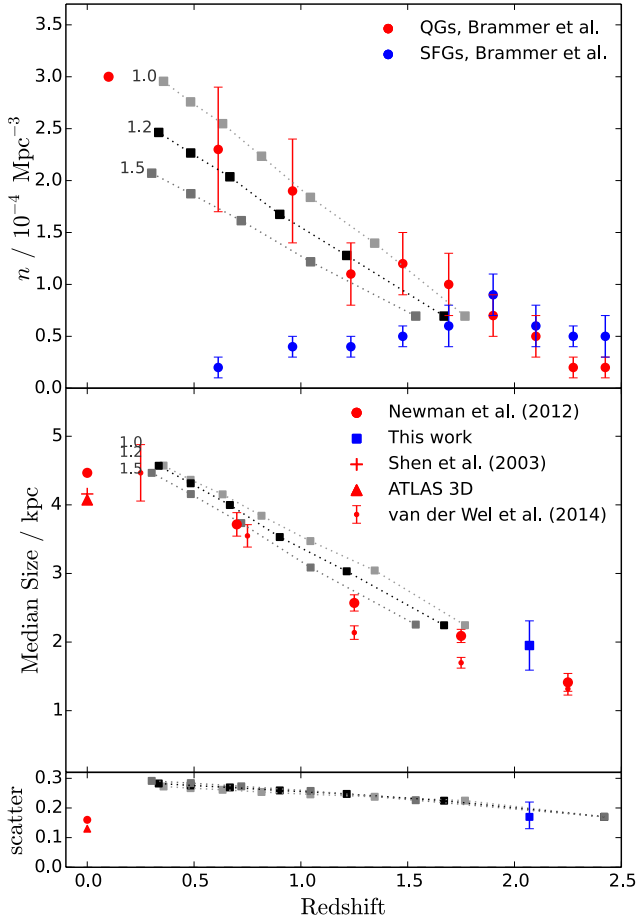


Figure 6. (*Top*) Number density evolution with redshift. The red and blue points show the observed number densities for quiescent and star-forming galaxies, respectively, with masses $\log(M/M_{\odot}) > 11$ from Brammer et al. (2011). The black and grey, connected points indicate our modeled evolution with varying quenching time indicated in Gyr by the small number at each line. (*Middle*) Average size of the quiescent galaxy population at fixed mass of $10^{11} M_{\odot}$ as function of redshift. The black and grey points are the same as in the top plot. The various points show other literature data. (*Bottom*) Modelled scatter as a function of redshift relative to the initial scatter of 0.20 dex at redshift $z = 2.4$, the first redshift-bin from Brammer et al. (2011). The evolution in number density and size is very well matched by the model. However, the scatter of the population increases with time contrary to what is observed.

ing times indicated in Gyr by the number at each of the tracks. The middle panel shows the evolution in average size of the sample of quiescent galaxies. Data from Newman et al. (2012) is shown in red circles, our sample is indicated by the blue square, and the local size measurements from Shen et al. (2003) and ATLAS^{3D} are shown by the red plus and triangle, respectively. Again, the black and grey points indicate the modeled evolution at different quenching times. The bottom panel shows the evolution of the scatter, σ , of the distribution of quiescent galaxies relative to the initial value at $z = 2.45$.

From these assumptions, we are able to reproduce the observed increase in number density and size of quiescent galaxies. However, the modelled scatter *increases* by ~ 0.15 dex on average towards lower redshifts in contrast with the constant scatter observed in this work and by van der Wel et al. (2014).

7. DISCUSSION

The evolution of galaxies in the mass–size plane is undoubtedly influenced by merging, star-formation and its cessation. As we increase the samples of well-studied, spectroscopically confirmed galaxies over a range of redshifts we can forge new diagnostic tools to address the weight with which each of these processes influences the evolution of galaxies.

In Sect. 6, we investigated the relation between stellar mass and half-light radius by parametrizing the relationship with a power-law. From the best fit to our quiescent grism sample, we found the slope, $\beta = 0.53$, and the scatter, $\sigma_{\log r_e} = 0.17$ dex, consistent with their $z = 0$ values. From the ATLAS^{3D} data and from a large SDSS sample from the work of Shen et al. (2003), Guo et al. (2009) and Newman et al. (2012), a local slope and scatter of $\beta_0 = 0.56 - 0.70$ and $\sigma_0 = 0.13 - 0.16$ dex was inferred. One complication in comparing samples of galaxies at different redshifts, and from different samples, lies in the fact that the distinction between star-forming and quiescent galaxies becomes less clear at higher redshifts. Various studies use different criteria to define quiescence, e.g., a cut in morphology, sSFR or rest-frame colors, which makes comparison between different datasets non-trivial. Even at low redshift, the classification of early type galaxies is performed in different ways.

The importance of a clean separation and definition of star-forming and quiescent galaxies becomes clear when we look at the scatter as a tool to unravel the evolution in the mass–size relation, since the scatter is highly sensitive to outliers. Newman et al. (2012) find a scatter of $\sigma_{\log r_e} = 0.26$ dex for galaxies at redshifts $2.0 < z < 2.5$, much higher than what we find in our data. The large scatter observed in the Newman et al. sample may be due, at least partly, to the uncertainty in photometric redshifts and contamination from star-forming galaxies.

7.1. Mechanisms for size growth

In large photometric samples it has also been shown that the slope of the mass–size relation evolves very little from $z \sim 2$ to $z \sim 0.2 - 0.4$ despite there being strong redshift evolution of the galaxy distribution in the mass–size plane (primarily a shift to larger sizes, see Newman et al. 2012, McLure et al. (2013), and van der Wel et al. (2014)). While the unchanging slope may be theoretically plausible as the slope may reflect initial formation rather than subsequent evolution (Ciotti, Lanzoni, & Volonteri 2007), the lack of evolution in the scatter observed in this work and in the work of van der Wel et al. (2014) is puzzling. The scatter about the mean mass–size relation should evolve with redshift according to the underlying physical driver for the evolution in the mass–size plane, i.e., merging, quenching, or further star formation.

Merging will typically move galaxies to higher masses and larger radii, with the direction and amplitude of the change in the mass–size plane determined by the mass ratio, orbital parameters and gas content of the merger (Naab, Johansson, & Ostriker 2009). In gas-rich mergers, the remnant may become more compact due to the gas falling to the center, which leads to strong star formation activity (Shankar et al. 2013). Star formation at later

times (e.g., merger induced) will increase the mass, alter the size depending on the location of the star formation, and will decrease the mean age of the sample of *quiescent* galaxies at subsequent redshifts.

Quenching of star-forming galaxies will conserve mass while the individual galaxy sizes may even slightly decrease (as low-surface brightness star-forming regions fade) but is operating on a separate galaxy population that has intrinsically larger sizes than most of the quiescent galaxies already in place (Khochfar & Silk 2006). The addition of these quenched galaxies will then drive the evolution of the mean size of the whole population without changing the individual galaxies that have already been quenched. However, it is still not entirely clear what happens to star-forming galaxies after they stop forming stars in terms of morphology and size; star-forming galaxies show a variety of morphologies but the quiescent population is more dominated by spheroidal morphologies.

7.2. Evolution of the scatter in sizes

Each of the above processes, in addition to directing the mass–size evolution, will affect the observed scatter of the mass–size relation and its evolution in different ways. Merging has been shown by Nipoti et al. (2012) to increase the scatter in the mass–size relation. The authors show that size evolution within a dissipationless (“dry”) merger-only scenario leads to significantly higher scatter than is observed at $z = 0$ (Nipoti, Treu, Leauthaud, Bundy, Newman, & Auger 2012). Mergers are certainly on-going between $z = 2$ and $z = 0$ and Nipoti et al. conclude that there must be a finely tuned balance between the different processes in their merging model in order to reproduce the tight observed relation at $z = 0$. This type of fine tuning is not a general characteristic of the galaxy population(s) and is extremely unlikely to persist in real-world systems. However, the models by Nipoti et al. 2012 only consider dry mergers of spheroids, which given the diverse population of galaxies at high redshift is an unrealistic scenario. More recently, Shankar et al. (2013) study the size evolution of galaxies by running simulations taking into account the various galaxy-galaxy interactions. They find that the scatter in sizes remains constant at all times. However, they over predict the scatter by $\sim 40\%$.

In the case of “dilution” of the population via quenching, the scatter will increase due to the addition of a new population of larger, quiescent galaxies. By using our toy model (see Sect. 6.1) for the quenching case, we have shown that we are able to reproduce the observed increase in both number density and median size of quenched galaxies as functions of redshift out to $z \sim 2$, see Fig. 6. However, our model shows that the scatter should increase by up to ~ 0.15 dex in the redshift range, $0.4 < z < 2.5$. This is inconsistent with the observations presented here and by van der Wel et al. (2014), i.e., the observed scatter in sizes is consistent with being constant from redshift $z \approx 2$ to $z = 0$.

Carollo et al. (2013) have found similar results regarding the evolution of sizes and number density out to $z \sim 1$ assuming the dilution of the quiescent population by younger and larger galaxies. Other studies, however, have shown that quenched galaxies with younger ages are not significantly larger than older quenched galaxies

(e.g., Whitaker et al. 2012), as would be predicted in a “dilution” scenario. The results of Whitaker et al. (2012) are based on post-starburst galaxies split into “young” and “old” galaxies separated by colour cuts resulting in median ages of the two samples of 1 Gyr and 2 Gyr, respectively, and do not as such span a very large dynamic range in ages. Moreover, determinations of stellar ages are highly uncertain and depend strongly on metallicity, dust attenuation, and star-formation histories. The separation of “old” and “young” galaxies is thus not straightforward and introduces large uncertainties in sample selection.

So far, most studies have focused on the role of merging only, especially dry minor merging, as the driver of size evolution since this mechanism is very efficient in terms of increasing the size of a galaxy without adding too much mass to the system (McLure et al. 2013). However, Nipoti et al. (2009, 2012) find that dry merging in a Λ CDM cosmology is insufficient to explain the needed increase in size. As we show with our model for size evolution in Sect. 6.1, the addition of larger, quenched galaxies means that each individual galaxy needs to undergo less size-evolution. The combination of different galaxy-galaxy interactions, both gas-rich and gas-poor, may then regulate the size-evolution of individual systems such that the scatter remains constant through time. Also, individual systems must evolve at high redshift as such compact galaxies locally are very rare (Trujillo et al. 2009, 2014; van der Wel et al. 2014) and merging of galaxies is an obvious mechanism for this evolution (Damjanov et al. 2009; Taylor et al. 2010; van de Sande et al. 2011; Toft et al. 2012). A cascade of mergers is also the most likely way for galaxies to undergo morphological changes from clumpy and in some cases disc-like at high redshift to spheroidal at low redshift (Naab & Trujillo 2006; Ciotti et al. 2007; Wuyts et al. 2010). Belli et al. (2014a) study the evolution of galaxies at fixed velocity dispersion as the velocity dispersion has been shown to correlate with age, such that the older populations locally have higher velocity dispersions (Belli, Newman, & Ellis 2014a). They target galaxies at redshifts $0.9 < z < 1.6$ with a preselected spheroidal morphology. Assuming that the velocity dispersion does not change during the lifetime of a galaxy the authors find that individual galaxies must evolve significantly, and that size evolution driven by the addition of larger galaxies at later times is inconsistent with the velocity dispersion data. The preselection on morphology in the study by Belli et al., however, may introduce a bias against larger sizes since galaxies with high ellipticity or disk-like appearance on the sky would not be included. Stockton et al. (2014) find very low axis ratios for a sample five galaxies at $z \sim 0.5$ (all five having $b/a < 0.5$). This may indicate a disk-like or prolate nature of a large fraction of quiescent galaxies.

At higher redshifts, $z > 2$, Belli et al. (2014b) use similar methods to study the evolution of galaxies at fixed velocity dispersion (Belli, Newman, Ellis, & Konidaris 2014b). Though their sample at high redshift is not complete, they conclude that a strong evolution of individual systems is needed in order to reconcile the high-redshift size-distribution with the locally observed distribution. Furthermore, the inferred size evolution happens at too high a rate compared to the expectations from dry, minor

merging (Oser et al. 2012; Nipoti et al. 2012). Newman et al. (2012) find consistent results, that is, at lower redshifts $z \lesssim 1$ the rate of size evolution is consistent with dry, minor merging, while at higher redshifts the size increase happens too fast to be driven purely by minor merging.

The fast increase in sizes at high redshift might be explained by the addition of larger, recently quenched galaxies as the number of star-forming galaxies at this epoch in cosmic time is comparable or even dominating. Under the assumption that the galaxy population turns off star formation more or less simultaneously, quenching of a big population of star-forming galaxies (in comparison to the size of the passive population in place) will cause a large increase in the median size of the distribution of quiescent galaxies, see Sect. 6.1. This effect will be stronger at higher redshifts when the number density of star-forming galaxies is high. At later times, $z \lesssim 1.5$, the quiescent population starts to dominate and hence the "dilution" effect contributes less. This is consistent with the scenario from Newman et al. and Belli et al., in which the size evolution of galaxies at lower redshifts is dominated by minor merging.

In order to study the evolution of galaxies and disentangle the various processes, high resolution, cosmological simulations are needed, which take into account both gas-rich and gas-poor galaxy interactions on the entire population of star-forming and quenched galaxies. These may be able to reproduce the lack of evolution in the scatter.

8. CONCLUSION

We have presented for the first time for a *spectroscopic* sample that the slope and scatter of the mass–size relation at $z = 2$ are consistent with their local values. We use the fact that the scatter remains constant from $z = 2$ to $z = 0$ as a tool to study the evolutionary mechanism that drives the size-increase of this population. We find that while the addition of larger galaxies quenched at later times can explain the increase of the average size of the population the scatter increases in contrast with the results presented here. Other processes, such as the combined influence from dry and wet mergers, is therefore needed to keep the scatter constant and to make the number density of the most compact galaxies evolve in a way that is consistent with their rarity in the local Universe.

The Dark Cosmology Centre is funded by the DNRF. JK acknowledges support from an ESO studentship. ST and AZ acknowledge support from the Lundbeck foundation. This work is based on observations taken by the 3D-HST Treasury Program (GO 12177 and 12328) with the NASA/ESA HST, which is operated by the Association of Universities for Research in Astronomy, Inc., under NASA contract NAS5-26555. This work is based on observations taken by the CANDELS Multi-Cycle Treasury Program with the NASA/ESA *HST*, which is operated by the Association of Universities for Research in Astronomy, Inc., under NASA contract NAS5-26555.

APPENDIX

THE DISCARDED SPECTRA

The discarded spectra can be grouped into the following categories:

- (i) spectra with bad background subtraction
#133784, #133915, #207144. These have breaks in the blue side of the spectra which could not be corrected for.
- (ii) spectra that are heavily noise dominated where more than half the pixels have $\text{SNR} < 1$:
#123780, #124168.
- (iii) highly contaminated:
#132654, #126073.
- (iv) flux-calibration issues, i.e., mismatch between the photometric J and H band:
#119753, #134172.
- (v) targets that fall outside our sample criteria after adding the spectral data to the fits:
#124686, #126301, #135214, #204878, #127617.

The target #127617 presents a strong and broad emission line in the spectrum, which indicates that this is not a passively evolving galaxy. We therefore remove it from our sample. The others in the category fall below the redshift definition when the spectra were fitted together with the photometry.

For the following targets, no spectra were extracted:

#123324, #123817, #126952, #128977, #139823, and #207084.

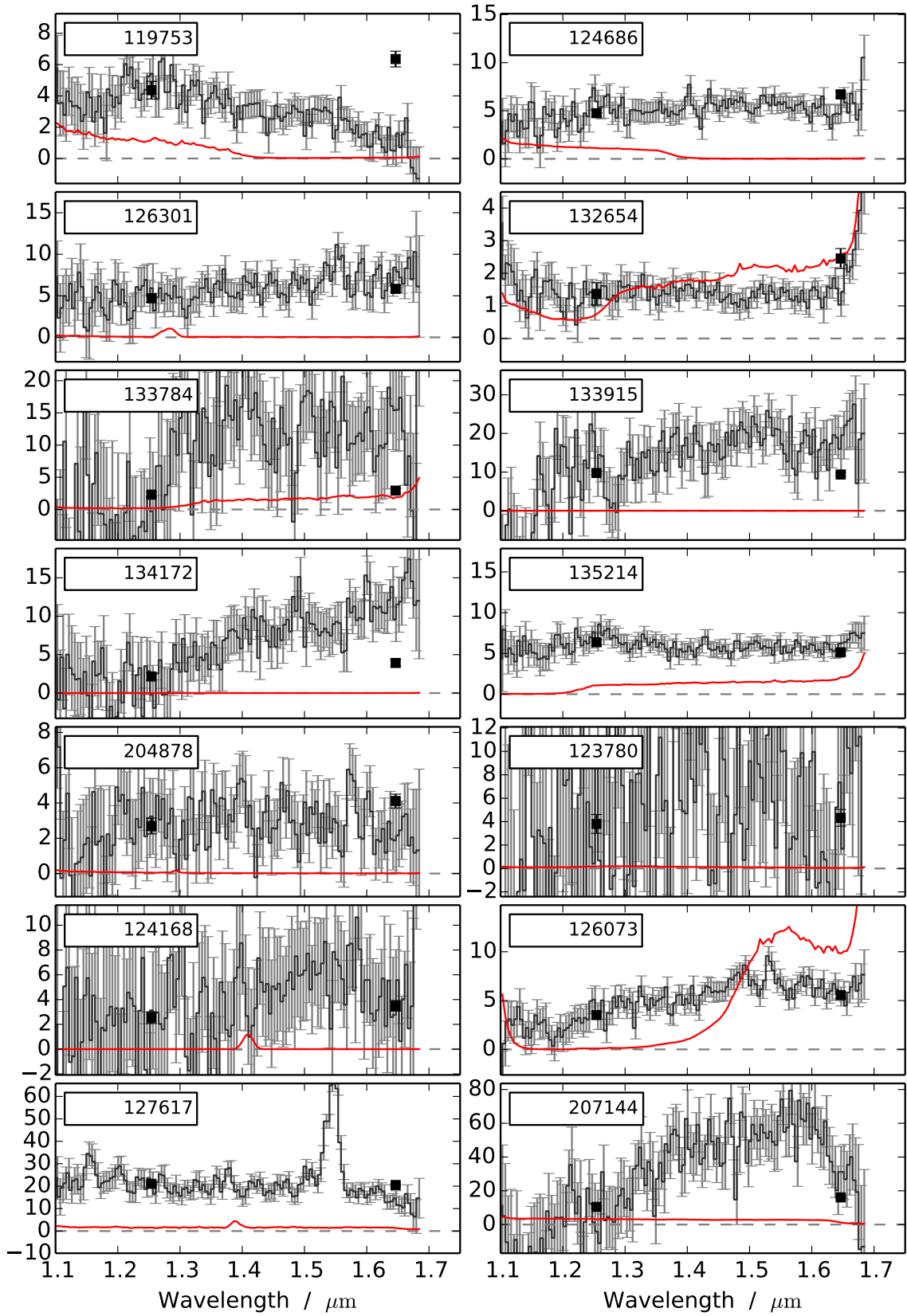


Figure 7. Discarded spectra from the sample, for individual notes see text. The spectra are shown as black with grey error bars in units of $10^{-19} \text{ erg}^{-1} \text{ s}^{-1} \text{ cm}^{-2} \text{ \AA}^{-1}$. The red line shows the contamination estimate.

GALFIT RESULTS

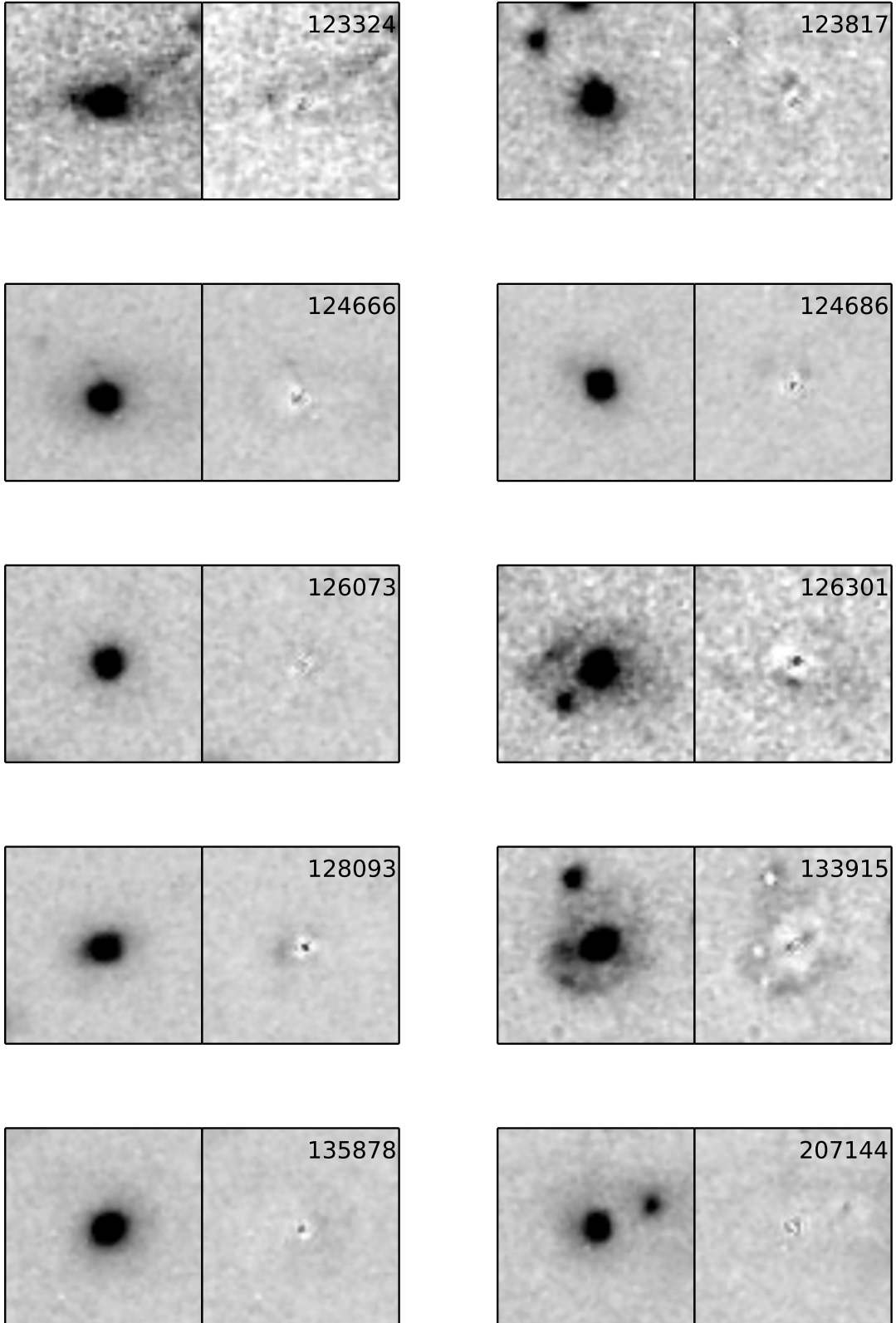


Figure 8. H_{160} images from the CANDELS data (*left*) and the residuals after subtracting the best-fit GALFIT model (*right*).

REFERENCES

- Bedregal, A. G., et al. 2013, *ApJ*, 778, 126
- Belli, S., Newman, A. B., & Ellis, R. S. 2014a, *ApJ*, 783, 117
- Belli, S., Newman, A. B., Ellis, R. S., & Konidaris, N. P. 2014b, *ApJ*, 788, L29
- Bezanson, R., van Dokkum, P. G., Tal, T., Marchesini, D., Kriek, M., Franx, M., & Coppi, P. 2009, *ApJ*, 697, 1290
- Brammer, G. B., et al. 2012, *ApJS*, 200, 13
- . 2011, *ApJ*, 739, 24
- Bruce, V. A., et al. 2012, *MNRAS*, 427, 1666
- Bruzual, G., & Charlot, S. 2003, *MNRAS*, 344, 1000
- Bruzual A., G. 1983, *ApJ*, 273, 105
- Buitrago, F., Trujillo, I., Conselice, C. J., Bouwens, R. J., Dickinson, M., & Yan, H. 2008, *ApJ*, 687, L61
- Cappellari, M., et al. 2011, *MNRAS*, 413, 813
- . 2013, *MNRAS*, 432, 1709
- Carollo, C. M., et al. 2013, *ApJ*, 773, 112
- Cassata, P., et al. 2011, *ApJ*, 743, 96
- Chabrier, G. 2003, *Publications of the Astronomical Society of the Pacific*, 115, 763
- Chevanche, M., Weijmans, A.-M., Damjanov, I., Abraham, R. G., Simard, L., van den Bergh, S., Caris, E., & Glazebrook, K. 2012, *ApJ*, 754, L24
- Ciotti, L., Lanzoni, B., & Volonteri, M. 2007, *ApJ*, 658, 65
- Daddi, E., Cimatti, A., Renzini, A., Fontana, A., Mignoli, M., Pozzetti, L., Tozzi, P., & Zamorani, G. 2004, *ApJ*, 617, 746
- Daddi, E., et al. 2005, *ApJ*, 626, 680
- Damjanov, I., et al. 2011, *ApJ*, 739, L44
- . 2009, *ApJ*, 695, 101
- Fan, L., Lapi, A., De Zotti, G., & Danese, L. 2008, *ApJ*, 689, L101
- Franx, M., et al. 2003, *ApJ*, 587, L79
- Franx, M., van Dokkum, P. G., Schreiber, N. M. F., Wuyts, S., Labbé, I., & Toft, S. 2008, *ApJ*, 688, 770
- Gobat, R., et al. 2013, arXiv:1305.3576
- Grogin, N. A., et al. 2011, *The Astrophysical Journal Supplement Series*, 197, 35
- Guo, Y., et al. 2009, *MNRAS*, 398, 1129
- Hopkins, P. F., Somerville, R. S., Hernquist, L., Cox, T. J., Robertson, B., & Li, Y. 2006, *ApJ*, 652, 864
- Khochfar, S., & Silk, J. 2006, *ApJ*, 648, L21
- Koekemoer, A. M., et al. 2011, *The Astrophysical Journal Supplement Series*, 197, 36
- Kriek, M., van Dokkum, P. G., Franx, M., Illingworth, G. D., & Magee, D. K. 2009a, *ApJ*, 705, L71
- Kriek, M., et al. 2008, *ApJ*, 677, 219
- Kriek, M., van Dokkum, P. G., Labbé, I., Franx, M., Illingworth, G. D., Marchesini, D., & Quadri, R. F. 2009b, *ApJ*, 700, 221
- Man, A. W. S., Toft, S., Zirm, A. W., Wuyts, S., & van der Wel, A. 2012, *ApJ*, 744, 85
- McLure, R. J., et al. 2013, *MNRAS*, 428, 1088
- Muzzin, A., et al. 2013, *ApJS*, 206, 8
- Naab, T., Johansson, P. H., & Ostriker, J. P. 2009, *ApJ*, 699, L178
- Naab, T., & Trujillo, I. 2006, *MNRAS*, 369, 625
- Newman, A. B., Ellis, R. S., Bundy, K., & Treu, T. 2012, *ApJ*, 746, 162
- Nipoti, C., Treu, T., Auger, M. W., & Bolton, A. S. 2009, *ApJ*, 706, L86
- Nipoti, C., Treu, T., Leauthaud, A., Bundy, K., Newman, A. B., & Auger, M. W. 2012, *MNRAS*, 422, 1714
- Onodera, M., et al. 2010, *ApJ*, 715, L6
- . 2012, *ApJ*, 755, 26
- Oser, L., Naab, T., Ostriker, J. P., & Johansson, P. H. 2012, *ApJ*, 744, 63
- Patel, S. G., et al. 2013, *ApJ*, 766, 15
- Poggianti, B. M., et al. 2013, *ApJ*, 762, 77
- Shankar, F., Marulli, F., Bernardi, M., Mei, S., Meert, A., & Vikram, V. 2013, *MNRAS*, 428, 109
- Shen, S., Mo, H. J., White, S. D. M., Blanton, M. R., Kauffmann, G., Voges, W., Brinkmann, J., & Csabai, I. 2003, *MNRAS*, 343, 978
- Stockton, A., Canalizo, G., & Maihara, T. 2004, *ApJ*, 605, 37
- Stockton, A., McGrath, E., Canalizo, G., Iye, M., & Maihara, T. 2008, *ApJ*, 672, 146
- Stockton, A., Shih, H.-Y., Larson, K., & Mann, A. W. 2014, *ApJ*, 780, 134
- Szomoru, D., Franx, M., & van Dokkum, P. G. 2012, *ApJ*, 749, 121
- Szomoru, D., et al. 2010, *ApJ*, 714, L244
- Tanaka, M., et al. 2013, *ApJ*, 772, 113
- Taylor, E. N., Franx, M., Glazebrook, K., Brinchmann, J., van der Wel, A., & van Dokkum, P. G. 2010, *ApJ*, 720, 723
- Toft, S., Franx, M., van Dokkum, P., Förster Schreiber, N. M., Labbe, I., Wuyts, S., & Marchesini, D. 2009, *ApJ*, 705, 255
- Toft, S., Gallazzi, A., Zirm, A., Wold, M., Zibetti, S., Grillo, C., & Man, A. 2012, *ApJ*, 754, 3
- Toft, S., et al. 2007, *ApJ*, 671, 285
- Trujillo, I., Carrasco, E. R., & Ferré-Mateu, A. 2012, *ApJ*, 751, 45
- Trujillo, I., Cenarro, A. J., de Lorenzo-Cáceres, A., Vazdekis, A., de la Rosa, I. G., & Cava, A. 2009, *ApJ*, 692, L118
- Trujillo, I., Ferré-Mateu, A., Balcells, M., Vazdekis, A., & Sánchez-Blázquez, P. 2014, *ApJ*, 780, L20
- Trujillo, I., et al. 2006, *ApJ*, 650, 18
- van de Sande, J., et al. 2013, *ApJ*, 771, 85
- . 2011, *ApJ*, 736, L9
- van der Wel, A., et al. 2012, *ApJS*, 203, 24
- . 2014, *ApJ*, 788, 28
- . 2011, *ApJ*, 730, 38
- van Dokkum, P. G., et al. 2008, *ApJ*, 677, L5
- van Dokkum, P. G., Kriek, M., & Franx, M. 2009, *Nature*, 460, 717
- van Dokkum, P. G., et al. 2010, *ApJ*, 709, 1018
- Weinzirl, T., et al. 2011, *ApJ*, 743, 87
- Whitaker, K. E., Kriek, M., van Dokkum, P. G., Bezanson, R., Brammer, G., Franx, M., & Labbé, I. 2012, *ApJ*, 745, 179
- Williams, R. J., Quadri, R. F., Franx, M., van Dokkum, P., & Labbé, I. 2009, *ApJ*, 691, 1879
- Williams, R. J., Quadri, R. F., Franx, M., van Dokkum, P., Toft, S., Kriek, M., & Labbé, I. 2010, *ApJ*, 713, 738
- Wuyts, S., Cox, T. J., Hayward, C. C., Franx, M., Hernquist, L., Hopkins, P. F., Jonsson, P., & van Dokkum, P. G. 2010, *ApJ*, 722, 1666
- Wuyts, S., et al. 2007, *ApJ*, 655, 51
- Zirm, A. W., et al. 2007, *ApJ*, 656, 66